# Inflammation potentiates JMML-like blood defects in Shp2 mutant Noonan syndrome

**Maja Solman[1], Sasja Blokzijl-Franke[1], Chuan Yan[4,5,6,7], Qiqi Yang[4,5,6,7], Sarah M. Kamel[1], Jeroen Bakkers[1,3], David M. Langenau[4,5,6,7], Jeroen den Hertog[1,2,*]**

Affiliations:

[1] Hubrecht Institute-KNAW and UMC Utrecht, 3584 CT Utrecht, the Netherlands

[2] Institute of Biology Leiden, Leiden University, 2333 BE Leiden, The Netherlands

[3] Department of Medical Physiology, Division of Heart and Lungs, UMC Utrecht, 3584 CX Utrecht, the Netherlands

[4] Molecular Pathology Unit, Massachusetts General Hospital Research Institute, Charlestown, MA 02129, United States of America

[5] Massachusetts General Hospital Cancer Center, Charlestown, MA 02129, United States of America

[6] Center for Regenerative Medicine, Massachusetts General Hospital, Boston, MA 02114, United States of America

[7] Harvard Stem Cell Institute, Cambridge, MA 02139, United States of America

* Correspondence: j.denhertog@hubrecht.eu

# Summary

The RASopathy Noonan syndrome (NS) is a frequent developmental disorder predominantly caused by activating mutations in the phosphatase SHP2. Among other features, NS children are predisposed to develop juvenile myelomonocytic leukemia (JMML). We developed a zebrafish mutant line carrying the NS-patient associated mutation Shp2-D61G. Shp2$^{D61G}$ zebrafish recapitulate major NS traits, including a JMML-like phenotype originating from defective hematopoietic stem and progenitor cells (HSPCs). Single cell RNA sequencing of mutant HSPCs revealed expansion of monocyte/macrophage progenitor cells associated with developmentally regulated cytokine production and elevated inflammation. Importantly, an anti-inflammatory agent rescued the JMML-like phenotype. Our results reveal a role for developmentally-induced inflammation in genesis of NS/JMML blood phenotypes and suggest anti-inflammatory drugs as potential new therapies.



# Keywords:

RASopathies, Noonan syndrome, Shp2, Zebrafish, JMML, HSPCs, scRNA-Seq, Inflammation

# Introduction

RAS signaling plays a central role in fundamental cellular processes, such as proliferation, cellular growth and differentiation, and is frequently altered during oncogenesis (Sanchez-Vega et al., 2018). Additionally, germline mutations in components of the RAS pathway are associated with a group of developmental disorders, termed RASopathies (Rauen, 2013; Tajan et al., 2018). The most common RASopathy is Noonan syndrome (NS), affecting 1:1,500 individuals (Roberts et al., 2013). NS has a systemic impact on development, causing short stature, congenital heart defects (predominantly pulmonary valve stenosis) and specific craniofacial characteristics, such as hypertelorism, low set ears and webbed neck. NS is a dominant autosomal disorder and 50% of NS patients carry heterozygous mutations in the protein-tyrosine phosphatase SHP2 (*PTPN11*), which is a positive regulator of RAS signaling (Gelb and Tartaglia, 2006; Tajan et al., 2015; Tartaglia et al., 2001). Most of the mutations are affecting residues found at the N-SH2/PTP interface, disrupting the autoinhibitory allosteric regulatory mechanism and consequently increasing the basal activity of SHP2 (Tajan et al., 2015; Tartaglia et al., 2002). Importantly, D61 is one of the most commonly mutated residues found in Noonan syndrome patients (Matozaki et al., 2009; Tartaglia et al., 2001).

A portion of NS children develop a hematological malignancy resembling juvenile myelomonocytic leukemia (JMML)-like myeloproliferative disease (MPD) (NS/JMML-like MPD), which in several cases is reported to self-resolve over time. However, in a minority of cases it progresses into the aggressive and often fatal JMML form (NS/JMML) (Niemeyer and Flotho, 2019; Strullu et al., 2014). NS/JMML-like MPD and

NS/JMML phenotypes are most commonly present in patients carrying a mutation in SHP2 (Kratz et al., 2005; Strullu et al., 2014). JMML is characterized by excessive proliferation of the monocyte and macrophage lineage and hypersensitivity of myeloid progenitors to granulocyte-macrophage colony stimulating factor (GM-CSF) (Chang et al., 2014; Emanuel et al., 1991). Other blood lineages also seem to be affected, since patients, in addition to monocytosis, often present with thrombocytopenia, anemia and increased fetal hemoglobin (HbF) levels (Locatelli and Niemeyer, 2015). NS/JMML-like MPD and NS/JMML are considered to be polyclonal diseases arising from multipotent hematopoietic stem cells (HSCs). However, little is known about the mechanisms that remodel the hematopoietic stem and progenitor cells (HSPCs) compartment during early pathogenesis.

Zebrafish (*Danio rerio*), having a conserved RAS signaling network, rapid development, transparent embryos, and a capacity for *in vivo* drug screens, serves as a robust tool to study the effect of mutations found in RASopathies on various developmental lineages (Jindal et al., 2015; Patterson and Burdine, 2020)**.** Ectopic expression of NS-associated mutants affects zebrafish embryonic development profoundly, inducing shorter body axis length, craniofacial defects, defective gastrulation and impaired heart looping (Bonetti et al., 2014; Jopling et al., 2007; Niihori et al., 2019; Paardekooper Overman et al., 2014; Runtuwene et al., 2011). Despite the development of gene editing technologies, knock-in of mutations into the endogenous locus remains challenging in zebrafish (Liu et al., 2019) and studying the effects of RASopathies-associated activating mutations still relies on ubiquitous overexpression of mutant proteins.

Here we describe a novel genetic zebrafish model of NS, which carries the patient associated Shp2$^{D61G}$ mutation at the endogenous locus, and reconstitutes major NS-associated traits. Interestingly, embryos of the Shp2$^{D61G}$ zebrafish developed hematological defects originating in defective HSPCs and resembling NS/JMML. Transcriptomic changes in mutant HSPCs from zebrafish embryos were explored using single cell RNA sequencing. A proinflammatory gene expression and cytokine production during early priming of the expanded population of mutant monocyte/macrophage progenitor cells was identified. Strikingly, anti-inflammatory drug treatment led to a partial reversal of the NS/JMML-like phenotype, emphasizing the role of the mutant Shp2 evoked inflammatory program in the monocyte/macrophage primed population of cells in NS/JMML pathogenesis.

# Results

### Novel Shp2$^{D61G}$ mutant generated by CRISPR/Cas9 mediated knock-in

The zebrafish genome contains two *ptpn11* genes (*ptpn11a* and *ptpn11b*), encoding Shp2a and Shp2b. Shp2a is indispensable during zebrafish development, whereas loss of Shp2b function does not affect development (Bonetti et al., 2014). Here we established a zebrafish genetic model of Noonan syndrome by knock-in of a patient-associated mutation in codon 61 (Asp to Gly) of the zebrafish ptpn11a gene. We used the recently described strategy of a CRISPR/Cas9-mediated homology directed repair (HDR) approach (**Supplemental Figure S1A**) (Tessadori et al., 2018). The efficiency of the knock-in was 1.8% (1 founder zebrafish in 54 screened primary injected zebrafish). The oligonucleotide used for the homology repair is 59 nucleotides long and besides the D61G mutation, contains three additional silent mutations in proximity of the PAM site (**Figure 1A**). Sequencing confirmed that the oligonucleotide was incorporated correctly into the genome (**Figure 1A**). Furthermore, the introduced mutations did not have a detectable effect on Shp2a protein expression (**Figure 1B**). Prior to phenotypical analyses, the mutant lines were outcrossed twice to ensure that potential background mutations due to the CRISPR/Cas9 approach were removed. Henceforth, the mutant zebrafish line we developed will be referred to as Shp2$^{D61G}$ mutant and when necessary Shp2$^{D61G/wt}$ and Shp2$^{D61G/D61G}$ mutant to further specify hetero- and homozygosity, respectively.

**Shp2$^{D61G}$ mutant zebrafish display typical Noonan syndrome traits**

The effect of the Shp2-D61G mutation was obvious during early development in 32% and 45% of 5 days post fertilization (dpf) old Shp2$^{D61G/wt}$ and Shp2$^{D61G/D61G}$ embryos, respectively (**Figure 1D**). The observed phenotypical defects were mostly mild, but in some cases severe defects were found, including severely stunted growth, edemas of the heart and jaw, and absence of the swim bladder (**Figure 1C**). Since the mutant embryos were mostly mildly affected, just as the NS patients, we performed more meticulous characterization of the typical NS traits. Body axis length was significantly reduced in Shp2$^{D61G}$ mutant embryos at 5dpf (**Figure 1E**). Furthermore, imaging of Alcian blue stained cartilage revealed NS-reminiscent craniofacial defects in the 4dpf Shp2$^{D61G}$ mutant embryos, characterized by broadening of the head (**Figure 1F**), leading to increased ratio of the width of the ceratohyal and the distance to Meckel's cartilage (**Figure 1G**). We also assessed the general morphology of the 3dpf embryonic hearts using whole-mount *in situ* hybridization (WISH) with cardiomyocyte (*myl7*), ventricular (*vhmc*) and atrial (*ahmc*) markers. There were no obvious morphological defects, such as change in the heart size or its looping, as well as the heart chamber specification at this stage (**Supplemental Figure S1B**). However, we obtained high speed video recordings of the Shp2$^{D61G}$ mutant hearts at 5dpf and performed functional heart analysis based on the ventricular kymographs derived from the recordings **(Figure 1H**)(Tessadori et al., 2012). Effects on cardiac function varied from embryo to embryo, which is reminiscent of variable heart defects in human patients. Overall, cardiac function was significantly affected in the Shp2$^{D61G}$ mutant

embryos, in particular a decrease in heart rate (**Figure 1I)**, ejection fraction and cardiac output (**Supplemental Figure** S**1C,D**).

Since most of the embryos with obvious phenotypical defects did not develop a swim bladder, they did not survive to adulthood, whereas the rest of both Shp2$^{D61G/wt}$ and Shp2$^{D61G/D61G}$ mutant zebrafish grew up normally. Adult Shp2$^{D61G}$ mutants displayed rather mild obvious defects, such as shorter body axis (**Figure 1J**), with markedly reduced length observed from the embryonic stage of 5dpf until the fully developed adults (**Figure 1K**). In 10% of Shp2$^{D61G}$ mutants the phenotypes were more severe (**Figure 1J**). These zebrafish mutants had markedly reduced body axis length compared to their siblings, they were skinny, with overall redness, especially in the head and gill region (**Figure 1J**).

Taken together, we have established a zebrafish model harboring a NS associated mutation. Shp2$^{D61G}$ mutant zebrafish phenocopied several of the typical NS traits, such as stunted growth, craniofacial defects, and heart defects.

**Shp2$^{D61G}$ zebrafish embryos develop NS/JMML-like phenotype**

NS/JMML-like MPD and NS/JMML phenotype are mostly linked to mutations in SHP2 (Kratz et al., 2005; Strullu et al., 2014). Thus, we explored hematopoietic abnormalities in the Shp2$^{D61G}$ zebrafish. Development of distinct hematopoietic lineages in Shp2$^{D61G}$ zebrafish embryos using lineage-specific markers was monitored. First, we investigated the effect of the Shp2$^{D61G}$ mutation on primitive hematopoiesis using WISH at 2dpf. We were not able to observe any difference in markers of erythroid progenitors (*gata-1*), myeloid progenitors (*pu.1*) and white blood cells (WBCs) (*l-plastin*), suggesting

that primitive hematopoiesis was not affected (**Supplemental Figure S2A**). On the other hand, a significant effect of the Shp2-D61G mutation on definitive hematopoiesis was observed, which was monitored at 5dpf (**Figure 2**). We observed an increase of *l-plastin* positive cells, marking all WBCs, in both caudal hematopoietic tissue (CHT) and head kidney region of the Shp2$^{D61G}$ mutants (**Figure 2A,B**). These cells appear not to be lymphocytes, since the size of the thymus stained with the marker for lymphoid cells, *ikaros*, was not affected (**Figure 2C,D**). By contrast, the myeloid lineage was markedly expanded, which was evident from the increase in the number of mpx-GFP positive cells, marking neutrophils (**Figure 2E,F**), and mpeg-mCherry positive cells, marking macrophages (**Figure 2E,G**), in the Tg(*mpx:GFP, mpeg:mCherry*) double transgenic mutant embryos. One of the clinical hallmarks of JMML is the hypersensitivity of myeloid progenitors to GM-CSF. In zebrafish, Gcsfa and Gcsfb stimulate growth and differentiation of colony forming unit-granulocyte (CFU-G) and of colony formation unit-macrophage (CFU-M) colony types, corresponding to the effects of GM-CSF in human (Svoboda et al., 2016). We cultured the whole kidney marrow (WKM) cells from Shp2$^{D61G}$ zebrafish and their wt siblings in the presence of Gcsfa and Gcsfb and evaluated colonies after 2 days. WKM cells from Shp2$^{D61G}$ zebrafish developed into colonies larger in size and number, demonstrating an enhanced GM colony forming ability (**Figure 2H,I)**. Additionally, a mild effect on the thrombocyte and erythroid blood lineage development was detected. Shp2$^{D61G}$ mutant embryos exhibit a decrease in the number of CD41-GFP$^{high}$ cells (**Figure 2J**), marking thrombocytes in the Tg(*cd41:GFP, kdrl:mCherry-CAAX*) transgenic line, and a decrease in *β-globin* positive cells, marking erythrocytes (**Figure 2K,L**). The observed defects on all different blood lineages

examined here were stronger in the homozygous Shp2$^{D61G/D61G}$ than heterozygous Shp2$^{D61G/wt}$ embryos, indicating a dose-dependent effect of Shp2-D61G protein.

Our findings suggest that similar to the effects observed in NS patients, the Shp2$^{D61G}$ mutant zebrafish embryos develop multilineage hematopoietic defects, with characteristics of increased output of the myeloid lineage, hypersensitivity to GM-CSF, mild anemia and thrombocytopenia, all in a Shp2-D61G dose dependent manner.

**NS/JMML-like phenotype has its origin in defective HSPCs and is dependent on both MAPK and AKT signaling**

NS/JMML-like MPD and NS/JMML are considered to have their origin in defective HSCs. Correspondingly, an increased number of HSPCs was observed in the CHT region of Shp2$^{D61G}$ zebrafish embryos, which were marked by CD41-GFP$^{low}$ in the Tg(*cd41*:*GFP*, *kdrl*:*mCherry-CAA*X) transgenic line **(Figure 3A,B)**. This was further supported by the increased *c-myb* signal, a marker of HSPCs, both in the CHT region and the head kidney of the mutant embryos **(Figure 3C,D)**. Shp2$^{D61G}$ mutation seems to affect both proliferation and apoptosis of HSPCs, evident by an increase in CD41-GFP cells positive for phosphohistone H3 (pHis3), a marker for late G2 and M phase and a decrease in Acridine orange positive cells in the CHT region, marking apoptotic cells (**Supplemental Figure S3A,B**).

Shp2 is known to mediate activation of both RAS-MAPK and PI3K signaling pathways. To determine whether the observed blood defects were driven by these pathways, *c-myb* and *l-plastin* markers were investigated by WISH in embryos treated continuously between 2 and 5dpf with either MEK inhibitor CI1040 or PI3K inhibitor

LY294002 (**Figure 3E**). MEK inhibitor led to strong inhibition of expansion of both HSPCs and myeloid lineage in mutant embryos (**Figure 3F,G**), indicating an essential role of the RAS-MAPK pathway in the observed defects. The PI3K pathway appeared to affect Shp2-D61G driven expansion of HSPCs strongly (**Figure 3G**), whereas its role in expansion of the myeloid lineage in mutant embryos was less prominent (**Figure 3F**).

Finally, we tested whether the observed myeloid expansion was reconstituted upon transplantation of the WKM cells harvested from Shp2$^{D61G/wt}$ animals in the Tg(*mpx:GFP, mpeg:mCherry*) background into the optically clear recipient *prkdc-/-* immunodeficient zebrafish(Moore et al., 2016a). Animals injected with mutant WKM cells (3/5) accumulated GFP- and mCherry- positive cells near the site of injection starting at 14 days and increasing until 28 days. By contrast, animals injected with WKM cells from control sibling animals with wt Shp2a (5/5) lacked any GFP- and mCherry-positive cells (**Figure 3H**).

These data indicate that the JMML-like blood defect developed in the Shp2$^{D61G}$ zebrafish has its origin in malignant HSPCs, is dependent on both MAPK and AKT signaling pathways and is transplantable into a secondary recipient.

**Myeloid bias is established during the early differentiation of Shp2$^{D61G}$ HSPCs**

In an effort to better understand the pathogenesis mechanisms in the Shp2$^{D61G}$ mutant HSPCs, single cell RNA sequencing was performed. CD41-GFP$^{low}$ cells were FACS sorted from the CHTs of 5dpf Shp2$^{wt}$, Shp2$^{D61G/wt}$ and Shp2$^{D61G/D61G}$ zebrafish embryos in the Tg(*cd41:GFP, kdrl:mCherry-CAAX*) transgenic background (**Figure 4A**). The number of cells for each genotype included in the analysis after the initial quality

control is indicated (**Figure 4B**). To group cells based on their transcriptional program, unsupervised clustering was performed using the RaceID3 package(Herman et al., 2018) and clusters were visualized by *t*-distributed stochastic neighbor embedding (*t*-SNE) (**Figure 4C)**. Identities of the 4 major clusters were determined based on the differentially expressed genes and GO term analysis (**Figure 4C, Supplemental Figure S4A, Supplemental Table S1**). Cells from cluster 2 expressed typical hematopoietic stem cell markers, such as *c-myb* and *her6* (*HES1* analogue in human) and were therefore considered the most HSC- like HSPCs (**Figure 4C, Supplemental Figure S4A**). Cluster 1 was characterized by expression of genes characteristic for thrombocyte and erythroid differentiation, such as *gata1a* and *klf1* and was therefore considered as thrombocyte and erythroid progenitors. Cells from cluster 3 represented early myeloid progenitors, characterized by expression of *runx3* and *cxcr4b* (**Figure 4C, Supplemental Figure S4A**). A small subset of cells in this cluster represented more differentiated neutrophils, recognized by high expression of genes such as *lyz* and *mpx* (**Supplemental Figure S4B**). We considered cells from cluster 4 as differentiating monocytes/macrophages, since they expressed genes typical for both lineages, such as *marco* and *ctsba* (**Figure 4C, Supplemental Figure 4A**).

HSPCs of either Shp2$^{wt}$ or mutant Shp2$^{D61G/wt}$ and Shp2$^{D61G/D61G}$ genotypes were present in all 4 major HSPCs compartments, indicating that distinct HSPCs phenotypes were maintained on a gene transcription level. However, the distribution of cells in clusters differed among genotypes. An overrepresentation of mutant Shp2$^{D61G/wt}$ and Shp2$^{D61G/D61G}$ cells was observed in the HSC-like HSPCs cluster and monocytes/macrophages progenitors cluster, whereas these were underrepresented in

the thrombocyte and erythroid progenitors **(Figure 4D,E**). To validate this observation, we investigated the expression of *pu.1* and *alas2* markers in Shp2$^{D61G}$ embryos of different genotypes by WISH. In the single cell RNA sequencing dataset, expression of *pu.1* and *alas2* was upregulated in the myeloid progenitors and erythroid progenitors, respectively (**Figure 4F,I**). An increased number of *pu.1* positive cells was detected by WISH in 5dpf old Shp2$^{D61G}$ embryos compared to their Shp2$^{wt}$ siblings (**Figure 4G,H**), whereas the number of *alas2* positive cells in Shp2$^{D61G}$ mutants was decreased (**Figure 4J,K**).

Taken together, single cell RNA sequencing suggests that defects during early HSPCs differentiation initiate the multilineage NS/JMML-like phenotype observed in Shp2$^{D61G}$ embryos.

**Excessive proinflammatory response contributes to the pathogenesis of the NS/JMML-like phenotype**

We further analyzed the cluster of monocyte/macrophage progenitors, in which we observed an overrepresentation of mutant Shp2$^{D61G}$ cells **(Figure 5A)**. Functional annotation of the differentially expressed genes and the GO-term enrichment analysis revealed presence of genes involved in inflammation (**Figure 5A, Supplemental Table S1**). Furthermore, among the top 10 differentially expressed genes was the inflammatory cytokine *il1b.* High levels of IL-1β have been previously detected in JMML(Bagby et al., 1988; Dong et al., 2016). Also other proinflammatory genes were highly expressed, such as *gcsfa, gcsfb, irg1, tnfaip3, nfkbiaa, ccl35.2* and *ccl34b.1* (**Figure 5A,B, Supplemental Table S1**). Interestingly, expression of inflammation-

related genes seemed to be constrained to the cells of mutant Shp2$^{D61G}$ genotype in the monocyte/macrophage progenitors cluster (**Figure 5A,B)**. For instance, there was a significant increase of the *gcsfa*, *gcsfb*, *il1b*, *irg1* and *nfkbiaa* gene expression in Shp2$^{D61G}$ cells, compared to the Shp2$^{wt}$ cells. On the other hand, a monocyte marker *timp2a* was equally expressed by cells of distinct genotypes (**Figure 5B)**.

The high expression of IL-1β in mutant embryos was further validated *in vivo*. The presence of IL-1β-eGFP positive cells was observed in the CHT region of Shp2$^{D61G}$ embryos in the Tg(*il1b:eGFP*, *mpeg:mCherry*) transgenic background (**Figure 5C)**. The IL-1β-eGFP positive cells overlapped partially with the branched cells that contained a high mpeg:mCherry signal, indicating macrophages, while the remaining IL-1β-eGFP positive cells were round in shape and contained little or no mpeg-mCherry signal.

Finally, we asked whether the excessive inflammatory response has a role in the pathogenesis of the observed phenotype. We exposed embryos to the anti-inflammatory corticosteroid dexamethasone continuously between 2 and 5dpf. A robust effect of the dexamethasone treatment on both expansion of myeloid lineage and HSPCs was observed, as determined by WISH for the *c-myb* and *l-plastin* markers (**Figure 5D,E)**.

These results show that the expanded monocyte/macrophage progenitors exhibited a pro-inflammatory phenotype and uncovered a profound role for inflammation in pathogenesis of NS/JMML. Strikingly, these monocyte/macrophage progenitors seem to have an essential role during initiation of the NS/JMML-like phenotype, in that an anti-inflammatory agent rescued the expansion of the myeloid lineage and HSPCs, revealing a new angle for combating (NS)/JMML.

# Discussion

Here, we focused on the hematological phenotype observed in Shp2$^{D61G}$ zebrafish embryos. In line with the characteristics typical for NS/JMML-like MPD and NS/JMML in human patients (Strullu et al., 2014), Shp2$^{D61G}$ embryos displayed expansion of the myeloid lineage, increased sensitivity to GM-CSF, mild anemia and thrombocytopenia **(Fig. 2)**. Furthermore, the observed blood defect was transplantable to secondary recipients and had its origin in the defective HSPCs compartment. A similar phenotype was observed in NS *Ptpn11*$^{D61G}$ mouse model, which develops NS/JMML-like MPD. However, these defects were observed in mice of 5 months old and they were never studied at the earlier, embryonic stages, which may be more relevant for disease initiation, since NS/JMML-like MPD and NS/JMML in patients appears at the very early age, often immediately after birth (Araki et al., 2004; Dong et al., 2016; Xu et al., 2010b). To uncover novel pathogenesis mechanisms during early HSPCs differentiation, we investigated the transcriptomes of these cells. The HSPCs compartment is heterogeneous, consisting of multipotent stem cells and progenitors of distinct blood lineages. Since in the Shp2$^{D61G}$ mutants multiple blood lineages are affected simultaneously, single cell RNA sequencing was performed in order to separate subpopulations of HSPCs and uncover subtle gene expression differences, which would not be possible by bulk sequencing. A single cell RNA sequencing dataset of the GFP-CD41$^{low}$ cells, corresponding to HSPCs, was generated both for Shp2$^{D61G}$ mutants and their wt siblings. The identities of HSPCs subpopulations matched the ones previously described (Athanasiadis et al., 2017), and they were all recognized in both Shp2$^{D61G}$ mutant and wt genotype. Remarkably, we observed an enrichment of

mutant HSPCs in the monocyte/macrophage progenitor cluster and their depletion in thrombocyte/ erythroid progenitor cluster, corresponding to phenotypes observed for the more differentiated blood lineages. The generated dataset represents a valuable resource for future studies on mechanisms involved in initiation of NS/JMML and NS/JMML-like MPD.

Our exploration of the differentially expressed genes in the cells of monocyte/macrophage progenitor cluster uncovered upregulation of pro-inflammatory genes specifically in the cells derived from Shp2$^{D61G}$ mutants **(Fig. 5)**. A proinflammatory status, with high levels of cytokines, such as IL-1β, TNF-α, GM-CFS, has been previously assigned to JMML in human patients and mouse models, and shown to be generated by myeloid cells (Bagby et al., 1988; Dong et al., 2016; Freedman et al., 1992; Hamarsheh et al., 2020; Zhao et al., 2018). The inflammatory response may be initiated in a cell autonomous way or in response to signals from the microenvironment. Dong et al. suggested that IL-1β is secreted by differentiated monocytes which get recruited upon the Chemokine (C-C motif) ligand 3 (CCL3) secretion by the cells of bone marrow microenvironment containing activating SHP2 mutations (Dong et al., 2016). However, the levels of CCL3 in the bone marrow of four NS patients varied. Our findings indicate that the proinflammatory status of the monocyte/macrophage lineage is initiated early during their differentiation. Hence, proinflammatory reprograming of the monocyte/macrophage lineage might be endogenously driven at least in part, and detailed mechanisms remain to be elucidated in the future. The role of inflammation as one of the drivers in myeloid leukemogenesis is emerging (Arranz et al., 2017; Craver et al., 2018). For instance, IL-1β is known to

induce proliferation of HSCs and their differentiation into the myeloid lineage (Dong et al., 2016; Pietras et al., 2016). Here we demonstrate that dampening inflammation using the glucocorticoid dexamethasone, partially rescued the observed blood phenotype in Shp2$^{D61G}$, suggesting that the inflammatory response evoked in the cells of myeloid/macrophage lineage is important driver of the NS/JMML-like blood defect and may be a potential drug target for (NS)/JMML and (NS)/JMML-like MPD.

Zebrafish is a particularly appealing model for NS, since it is possible to study early development directly in large numbers of transparent embryos, and it is amenable for performance of *in vivo* drug screens(Patterson and Burdine, 2020). However, a lack of zebrafish genetic models limits current studies to transient ubiquitous overexpression of the NS activating mutants in zebrafish embryos. Here, we report the first NS zebrafish model carrying a Shp2a-D61G mutation at its endogenous locus generated by CRISPR/Cas9- based knock-in technology. Strikingly, phenotypes developed by the Shp2$^{D61G}$ zebrafish corroborate closely with the phenotypes displayed by human NS patients and the existing NS mouse models **(Fig. 1)**. Shp2$^{D61G}$ embryos are shorter and they display defects in craniofacial development, heart function and hematopoiesis. A portion of both heterozygous and homozygous embryos develop normally to adulthood or are only mildly affected, while 10% show severe phenotype in the adult stages. In addition, phenotypes vary from one mutant zebrafish to another and they are more severe in the homozygotes, indicating a Shp2-D61G dose dependence. Our model presents an exciting novel tool for depicting pathogenesis mechanisms of NS with its complex traits and for finding novel therapies for this as yet poorly treatable condition.

Embryonic lethality is only partial in the Shp2$^{D61G}$ homozygous zebrafish, while in the NS Shp2$^{D61G}$ homozygous mice it is fully penetrant, due to severe heart valvoseptal defects (Xu et al., 2010a). Valvoseptal defects are also the most common cardiac defects in NS patients carrying a Shp2 mutation (Karnik and Geiger, 2019). Shp2$^{D61G}$ zebrafish displayed mild and severe heart edemas and changes in the heart rate, ejection fraction and cardiac output **(Fig. 1, Supplemental Fig. 1)**. However, striking heart malformations were not present; we did not observe major morphological changes or changes in the heart chamber specifications. More subtle effects could be present and a thorough assessment of the heart structure, focusing on valvoseptal components would be required to obtain a better insight in the future.

The observed difference in penetrance of embryonic lethality might be due to underlying genetic modifiers (Riordan and Nadeau, 2017). The genetic background of mice was shown to significantly affect embryonic lethality in distinct NS mouse models (Araki et al., 2009; Hernández-Porras et al., 2015). Hence, the genetic background might also be important in Shp2$^{D61G}$ zebrafish. Additionally, gene redundancy caused by the *ptpn11b* (Shp2b) paralogue in zebrafish, which is not present in the mouse or human genome (Bonetti et al., 2014) might rescue lethality in homozygous Shp2$^{D61G}$ zebrafish. However, we ruled out this possibility by crossing the Shp2$^{D61G}$ with *ptpn11b-/-* zebrafish. We did not observe any impact of Shp2b knock-out on the severity of the Shp2$^{D61G}$ phenotypes (data not shown).

In addition to the effect of anti-inflammatory treatment **(Fig. 5)**, we demonstrated that targeting MAPK and PI3K pathway also led to partial reversal of the blood phenotype in Shp2$^{D61G}$ zebrafish embryos **(Fig. 3e,f,g)**, further emphasizing previously

assigned role of these pathways in transformation of HSCs upon Shp2 activation (Pandey et al., 2017) and their therapeutic potential. Treatment of JMML and JMML-like MPD remains challenging, with no existing drug therapies. Our results emphasize the potential of the NS zebrafish model as a powerful tool for future *in vivo* drug screens.

# Acknowledgements

We thank the laboratory of Niels Geijsen (Hubrecht Institute) for providing us with Cas9 protein, Petr Bartunek and Olga Machanova (Institute of Molecular Genetics, Academy of Sciences of the Czech Republic v.v.i. Prague) and Geert Wiegertjes (University Wageningen) for cytokines and carp serum, Stefan van der Elst for assistance with FACS sorting, Hubrecht Institute animal caretakers for animal support and Single Cell Discoveries and Chloé Baron for support with single cell RNA sequencing. This work was supported by E-Rare grant NSEuroNet (JdH), NIH grants R01CA211734 (D.M.L) and R24OD016761 (D.M.L), the MGH Research Scholar Award (D.M.L.) and Alex Lemonade Stand Foundation (C.Y.).

# Author Contributions

**MS** Conceptualization, Methodology, Formal analysis, Investigation, Data Curation, Writing - Original Draft, Visualization

**SBF** Investigation, Formal analysis, Data Curation, Methodology, Writing - Review & Editing

**CY, QY** Investigation- performed transplantation experiments, Data Curation, Formal analysis, Methodology, Writing - Review & Editing

**SMK** Investigation- provided assistance with heart function analysis, Methodology, Resources, Writing - Review & Editing

**JB** Conceptualization, Supervision, Writing - Review & Editing

**DML** Conceptualization, Supervision, Writing - Review & Editing

**JDH** Conceptualization, Supervision, Funding acquisition, Project administration, Writing - Original Draft

## Competing Interest Statement

The authors declare no competing interests.

# Figure Titles and Legends

**Figure 1: Shp2$^{D61G}$ zebrafish display NS-like traits**

**(A)** Sequencing trace derived from Shp2$^{D61G/D61G}$ zebrafish. Oligonucleotide sequence used to generate the model is underlined. Nucleotide substitutions for D61G mutation (red), silent mutations (green) and the PAM site (blue) are indicated.

**(B)** Immunoblot of Shp2 levels from 5 pooled Shp2a$^{wt}$Shp2b$^{-/-}$ or Shp2a$^{D61G/D61G}$Shp2b$^{-/-}$ embryos using antibodies for Shp2 and tubulin (loading control).

**(C)** Representative images of typical Shp2$^{D61G}$ zebrafish embryonic phenotypes at 5dpf. Blue arrows: jaw, green arrows: heart, red arrows: swim bladder.

**(D)** Quantification of phenotypes of Shp2$^{wt}$, Shp2$^{D61G/wt}$ and Shp2$^{D61G/D61G}$ embryos scored as in (c) normal, mild and severe.

**(E)** Body axis length of Shp2$^{wt}$, Shp2$^{D61G/wt}$ and Shp2$^{D61G/D61G}$ embryos at 5dpf.

**(F)** Representative images of Alcian blue stained head-cartilage of 4dpf Shp2$^{wt}$ and Shp2$^{D61G/wt}$ embryos. (x) width of ceratohyal, (y) distance to Meckel's cartilage.

**(G)** Quantified craniofacial defects (x/y ratio).

**(H)** Representative ventricular kymographs derived from high speed video recordings of beating hearts of 5dpf Shp2$^{wt}$ and Shp2$^{D61G/wt}$ embryos. Red dotted lines indicate one heart period.

**(I)** Heart rates derived from the ventricular kymographs.

**(J)** Representative images of typical Shp2$^{D61G}$ zebrafish adult phenotypes at 24wpf. Scale bar is 0.5cm. Insets, zoom-in of boxed regions.

**(K)** Body axis lengths of 10 Shp2$^{wt}$, 25 Shp2$^{D61G/wt}$ and 10 Shp2$^{D61G/D61G}$ zebrafish measured weekly between 5dpf and 20wpf of age.

**(D,E,G,I)** Measurements originate from three distinct experiments. Number on bars: number of embryos. **(E,G,I,K)** Error bars: standard error of the mean (SEM), *p < 0.05; **p < 0.01, ANOVA complemented by Tukey HSD.

**Figure 2: Myeloid bias and increased sensitivity to Gcsfa,Gcsfb is observed in the Shp2$^{D61G/wt}$ zebrafish**

**(A)** WISH of 5dpf Shp2$^{wt}$ and Shp2$^{D61G/wt}$ embryos using *l-plastin* specific probe. Head kidney (arrow) and CHT (box) are indicated and zoom-in in insert. Scale bars, 150 μm.

**(B)** Quantification of *l-plastin* expression in Shp2$^{wt}$, Shp2$^{D61G/wt}$ and Shp2$^{D61G/D61G}$ embryos scored as low, mid and high.

**(C)** WISH of 5dpf Shp2$^{wt}$ and Shp2$^{D61G/wt}$ embryos using *ikaros* specific probe. Thymus is indicated (arrow).

**(D)** Size of *ikaros*-positive thymus.

**(E)** Representative images of Shp2$^{wt}$ and Shp2$^{D61G}$ zebrafish embryos in Tg(*mpx:GFP, mpeg:mCherry*) background at 5dpf. Mpx-GFP marks neutrophils and mpeg-mCherry macrophages. Scale bars, 150μm.

**(F,G)** Number of mpx-GFP and mpeg-mCherry positive cells.

**(H)** Representative images of colonies developed from WKM cells prepared from Shp2$^{wt}$, Shp2$^{D61G/wt}$ and Shp2$^{D61G/D61G}$ adult zebrafish, grown in methylcellulose with zebrafish cytokines Gcsfa and Gcsfb for 2 days. Scale bar, 20μm.

**(I)** Quantification of number of colonies from (h).

**(J)** Number of CD41-GFP$^{high}$ cells in Shp2$^{wt}$, Shp2$^{D61G/wt}$ and Shp2$^{D61G/D61G}$ zebrafish embryos at 5dpf were counted and percentage of embryos with either 0-50, 50-75 or 75-100 CD41-GFP$^{high}$ cells was plotted.

**(K)** WISH of 5dpf Shp2$^{wt}$ and Shp2$^{D61G/wt}$ embryos using *β-globin* specific probe. Scale bar, 150μm.

**(L)** Quantification of *β-globin* expression in Shp2$^{wt}$, Shp2$^{D61G/wt}$ and Shp2$^{D61G/D61G}$ embryos scored as low, mid and high.

**(B,D,F,G,J,L)** Measurements originate from at least three distinct experiments. Number on bars: number of embryos. **(E,I)** Error bars represent SEM. NS, not significant; *p < 0.05, ANOVA complemented by Tukey HSD.

**Figure 3: Shp2$^{D61G}$ induces JMML-like phenotype that originates in HSPCs, depends on MAPK and PI3K pathway and is transplantable into secondary recipient**

**(A)** Representative images of the CHT region of Shp2$^{wt}$ and Shp2$^{D61G}$ zebrafish embryos in the Tg(*cd41*:*GFP, kdrl:mCherry-CAAX*) background at 5dpf. CD41-GFP$^{low}$ cells mark HSPCs and CD41-GFP$^{high}$ cells thrombocytes. Scale bar, 20μm.

**(B)** The low intensity CD41-GFP positive cells in the CHT region were counted. Error bars represent standard error of the mean (SEM). *p < 0.05, ANOVA complemented by Tukey HSD.

**(C)** WISH of 5dpf Shp2$^{wt}$ and Shp2$^{D61G/wt}$ embryos using *c-myb* specific probe. Head kidney (arrow) and CHT (box) are indicated; zoom-in in insert. Scale bars, 150 μm.

**(D)** Quantification of *c-myb* WISH. *C-myb* expression in Shp2$^{wt}$, Shp2$^{D61G/wt}$ and Shp2$^{D61G/D61G}$ embryos was scored as low, mid and high.

**(E)** Schematic overview of the treatments with MEK inhibitor CI1040 and PI3K inhibitor LY294002. Embryos were continuously treated from 48hpf until 5dpf, when WISH was performed and expression of the **(F)** *l-plastin* and **(G)** *c-myb* marker was scored as low, mid and high. NS, not significant; *p < 0.05, **p<0.01, ***p<0.001, Chi-squared test.

**(H)** WKM cells harvested from Shp2$^{wt}$ and Shp2$^{D61G}$ zebrafish in the Tg(*mpx:GFP, mpeg:mCherry*) background were injected into the peritoneum of adult *prkdc*-/- zebrafish. Recipients were monitored by fluorescence imaging.

**(B,D,F,G)** Measurements originate from at least three distinct experiments. Number on bars: number of embryos.

**Figure 4: Transformation of Shp2$^{D61G}$ HSPCs studied by single cell RNA sequencing**

**(A)** Schematic representation of the experimental procedure. At 5dpf, CHTs from Shp2$^{wt}$, Shp2$^{D61G/wt}$ and Shp2$^{D61G/D61G}$ embryos in the Tg(*cd41*:*GFP, kdrl:mCherry-CAAX*) background were isolated. Cells were dissociated and separated by FACS, based on CD41-GFP$^{low}$ expression, prior to single cell RNA sequencing, as described in the Methods section.

**(B)** Number of cells of distinct genotypes used in single cell RNA sequencing analysis.

**(C)** tSNE maps generated using the cells of all three (Shp2$^{wt}$, Shp2$^{D61G/wt}$ and Shp2$^{D61G/D61G}$) genotypes. Single cells from 4 major clusters are marked in violet,

blue, pink and green and their identities based on marker gene expression are indicated. Minor clusters are marked in grey.

**(D)** Barplots showing the percentage of cells of Shp2$^{wt}$, Shp2$^{D61G/wt}$ and Shp2$^{D61G/D61G}$genotype in distinct clusters.

**(E)** Cells of distinct genotypes Shp2$^{wt}$, Shp2$^{D61G/wt}$ and Shp2$^{D61G/D61G}$ are visualized in tSNE maps in red.

**(F)** tSNE maps showing log2-transformed read-counts of *pu.1*.

**(G)** Representative images of the WISH staining for *pu.1* expression in 5dpf Shp2$^{wt}$ and Shp2$^{D61G}$ zebrafish embryos. Scale bar, 100 μm.

**(H)** Expression of the *pu.1* marker scored as low, mid and high.

**(I)** tSNE maps showing log2-transformed read-counts of *alas-2*.

**(J)** Representative images of the WISH staining for *alas-2* expression in the tail region of 5dpf Shp2$^{wt}$ and Shp2$^{D61G}$ zebrafish embryos. Scale bar, 100 μm.

**(K)** Expression of the *alas-2* marker scored as low, mid and high.

**(H,K)** Number on bars: number of embryos.

**Figure 5: Inflammatory response in monocyte/ macrophage progenitors in Shp2$^{D61G}$ embryos**

**(A)** The monocyte/macrophage progenitors cluster (boxed on the tSNE map on left) was analyzed in detail. log2-transformed sum of read-counts of selected inflammation-related genes from the top 50 differentially expressed genes in the cells of the monocyte/macrophage progenitors cluster, with genotype and number of cells (n) indicated above.

**(B)** Violin plots show the expression of specific genes in monocyte/macrophage progenitors of Shp2$^{wt}$, Shp2$^{D61G/wt}$ and Shp2$^{D61G/D61G}$ genotypes. NS, non significant, ***$p < 0.001$, t-test.

**(C)** *In vivo* imaging of the CHT region of Shp2$^{wt}$ and Shp2$^{D61G/wt}$ zebrafish embryos in the Tg(*il1b:eGFP*, *mpeg:mCherry*) background at 5dpf. Representative images are shown. Scale bar is 20μm.

Embryos were continuously treated from 48hpf until 5dpf with Dexamethasone, when WISH was performed and expression of the **(D)** *l-plastin* and **(E)** *c-myb* marker was scored as low, mid and high. Measurements originate from at least three distinct experiments. Number on bars: number of embryos. NS, not significant; *$p < 0.05$, **$p<0.01$, Chi-squared test.

# STAR Methods

## Resource Availability

### Lead Contact

Further information and requests for resources and reagents should be directed to and will be fulfilled by the Lead Contact, Jeroen den Hertog (j.denhertog@hubrecht.eu).

### Materials Availability

Zebrafish line generated in this study is available upon request.

### Data and Code Availability

For original data, please contact j.denhertog@hubrecht.eu. The accession number for the single cell RNA sequencing data reported in this study is GEO:

## Experimental model and subject details

### Ethics statement

All procedures involving experimental animals were approved by the animal experiments committee of the Royal Netherlands Academy of Arts and Sciences (KNAW), Dierexperimenten commissie protocol HI18-0702, and performed under the local guidelines in compliance with national and European law.

### Zebrafish husbandry

The following zebrafish lines were used in the study: Tübingen longfin (TL, wild type), Tg(*cd41:GFP, kdrl:mCherry-CAAX*)(Hogan et al., 2009; Lin et al., 2005), Tg*(mpx:GFP,*

*mpeg:mCherry)*(Ellett et al., 2011; Renshaw et al., 2006), TgBAC(*il1b:eGFP*)sh445(Ogryzko et al., 2018), *ptpn11b-/-*(Bonetti et al., 2014), *prkdc-/-* (Moore et al., 2016a) and the novel Shp2$^{D61G}$ zebrafish line. Raising and maintenance of zebrafish was performed according to (Monte Westerfield, 2000). When required, pigmentation of embryos was blocked by adding phenylthiourea (PTU) at a concentration of 0.003% (v/v) to the E3 medium at 24hpf.

## Methods Details

### Generation of the Shp2$^{D61G}$ zebrafish line

The Shp2$^{D61G}$ zebrafish line was generated using the previously described CRISPR/Cas9-based knock-in approach (Tessadori et al., 2018). The sgRNA targeting exon 3 of the *ptpn11a* gene (5'- GGAGACTATTACGACCTGTA-3') was designed using the CHOP-CHOP database (http://chopchop.cbu.uib.no/)**,** further processed according to the previously published guidelines (Gagnon et al., 2014) and finally transcribed using the Ambion MEGAscript T7 kit (TermoFisher Scientific). The sgRNA, constant oligonucleotide and template oligonucleotide were all generated by Integrated DNA Technologies (IDT) as standard desalted oligos and template oligonucleotide was further purified using the QIAquick Nucleotide Removal Kit (Qiagen). The sequence of template oligonucleotide is 5'-GAGTGGCAAACTTCTCTCCACCATATAAATCGTAATAGCCTCCTGTGTTTTGAATCTTA-3'. Tübingen longfin wt zebrafish embryos at the one-cell-stage were injected directly in the cell with 1 nl of the injection mixture containing 18.75 ng/ml of sgRNA, 37.5 ng/ml of template oligonucleotide and 3.6 mg/ml of Cas9 protein in 300 mM KCl.

Cas9 protein was a gift from the Niels Geijsen laboratory at the Hubrecht Institute. The injected embryos were grown into the adulthood. F0 generation zebrafish were outcrossed with the wt zebrafish. DNA extracted from the 12 distinct 1dpf old F1 generation embryos was screened for the correct insertion of the template oligonucleotide. Screening was done by Sanger sequencing (Macrogen) of the 225 bp long PCR product encompassing the genomic regions of the CRISPR target sites, which was generated using the forward 5'-TCATCTCCTCACTAGGCGAAAT-3' and reverse primer 5'- TATGTATGTGCTCACCTCTCGG-3'. F1 generation was then established from the F0 founder. F1 generation adults were finclipped and sequenced for the presence of the mutation. All experiments were performed in zebrafish embryos and adults from the F3 and F4 generation. For most of the experiments, embryos were derived from an incross of Shp2$^{D61G/wt}$ animals. After the experimental procedure, embryos were lysed and genotyped by sequencing as described above. Western blotting was performed as previously described (Hale and den Hertog, 2017) using the Shp2 (SC-280, Santa Cruz Technology) and β-tubulin (CP06, Merck Millipore) antibodies.

**Body length measurements**

Body axis lengths were measured from the tip of the head to the end of the trunk in the bright-field images of laterally positioned embryos, larva and adults, which were anesthetized in 0.1% MS-222 (Trycane, Sigma Aldrich).

**Alcian blue staining**

PTU-treated 4dpf old embryos were anesthetized in 0.1% MS-222 and fixed in 4% PFA overnight. Alcian blue staining was performed as described in (Paardekooper Overman et al., 2014). Embryos were positioned on their back in 70% glycerol in PBS and imaged with Leica M165 FC stereomicroscope (Leica Microsystems). Analysis was performed in ImageJ (U. S. National Institutes of Health, Bethesda, Maryland, USA).

### *In vivo* high-speed brightfield imaging of the embryonic hearts

PTU-treated embryos at 5dpf were anesthetized in 0.1% MS-222 and embedded in 0.3% agarose (UltraPure, Thermo Fisher Scientific) prepared in E3 medium containing 16 mg/ml MS-222. Measurements were performed at 28°C using a Leica DM IRBE inverted light microscope (Leica Microsystems) with a Hamamatsu C9300-221 high-speed CCD camera (Hamamatsu Photonics). Imaging was conducted at 150 frames per seconds (fps) using Hokawo 2.1 imaging software (Hamamatsu Photonics) for a period of 10 seconds (approximately 30 cardiac cycles). Heart rate measurements and contractility parameters were analysed using ImageJ. Volumes were analysed using ImageJ by drawing an ellipse on top of the ventricle at end-diastole and end-systole. Averages of three measurements per heart were determined. End diastolic and end systolic volume (EDV/ESV) were calculated by: (4/3)*(π)*(major axis/2)*((minor axis/2)^2). Stroke volume (SV) by: EDV-ESV. Ejection fraction (EF) by: (SV/EDV)*100. Cardiac output (CO) by: SV*Heart rate.

### Whole mount *in situ* hybridization

PTU-treated embryos were anesthetized in 0.1% MS-222 and fixed in 4% PFA for at least 12h at 4°C. *WISH* was performed as described in (Thisse et al., 1993)**.** Probes

specific for *myl7*, *vhmc* and *ahmc* were described in(Bonetti et al., 2014). Probes specific for *c-myb*, *l-plastin*, *pu.1*, *gata1*, *ikaros*, *b-globin* and *alas-2* were described in(Choorapoikayil et al., 2014; Hu et al., 2014)**.** Subsequently, embryos were mounted in 70% glycerol in PBS and imaged with Leica M165 FC stereomicroscope. Images were processed in ImageJ. Abundance of the probe signal was scored as low, mild or high.

**Confocal microscopy**

All confocal imaging was performed on a Leica SP8 confocal microscope (Leica Microsystems). Embryos were mounted in 0.3% agarose. Live embryos were anesthetized in MS-222. Whole embryos were imaged using a 10X objective and z-stack step size of 3μm, while the CHT area with 20X objective and z-stack step size of 1μm. The number of CD41-GFP$^{low}$ cells was determined by imaging the CHT of the living 5dpf old embryos of the Shp2$^{wt}$, Shp2$^{D61G/wt}$ and Shp2$^{D61G/D61G}$ siblings in the Tg(*cd41:GFP, kdrl:mCherry-CAAX*) transgenic background, while the number of CD41-GFP$^{high}$ cells was determined by imaging whole embryos, which were fixed for 2h in 4% PFA prior to imaging. To determine the number of mpx-GFP and mpeg-mCherry cells, whole live 5dpf old embryos of the Shp2$^{wt}$, Shp2$^{D61G/wt}$ and Shp2$^{D61G/D61G}$ line in the Tg*(mpx:GFP, mpeg:mCherry)* transgenic background were imaged. Imaris (Bitplane) was used to reconstruct 3D images and count individual GFP and/or mCherry positive cells.

**Phosphorylated Histone 3 (pHis3) staining**

PTU-treated 5dpf old Shp2$^{D61G}$ embryos in the Tg(*cd41:GFP, kdrl:mCherry-CAAX*) transgenic background were fixed in 2% PFA overnight and stained as described in (Choorapoikayil et al., 2012). Primary pHis3 antibody (1:500 in blocking buffer, Abcam) and secondary GFP antibody (1:200 in blocking buffer, Aves Labs Inc.) were used. Embryos were mounted in 0.3% agarose, their CHT was imaged using the SP8 confocal microscope and 3D images were subsequently reconstructed using Imaris.

**Acridine orange staining**

PTU-treated embryos at 5dpf were incubated in 5µg/ml of Acridine orange (Sigma Aldrich) in E3 medium, for 20 minutes at room temperature. They were then washed 5 times for 5 minutes in E3 medium, anesthetized in MS-222 and mounted in 0.3% agarose. Whole embryos were imaged with SP8 confocal microscope and 3D images were reconstructed using Imaris.

**Inhibitors treatment**

PTU-treated embryos were incubated with either 0.15µM of CI1040 (Sigma Aldrich), 4µM LY294002 (Sigma Aldrich) or 10µM of Dexamethasone (Sigma Aldrich) continuously from 24hpf until 5dpf. At 5dpf embryos were fixed and half of the embryos was processed for WISH using probe specific for *c-myb* and the other half using probe specific for *l-plastin*. Images were procefssed in ImageJ. Abundance of the probe signal was scored as low, mild or high.

**Isolation of CD41-GFP$^{low}$ cell population and single-cell RNA sequencing**

From 24hpf onwards embryos were grown in PTU-containing medium. The CHTs of approximately 50 Shp2$^{wt}$, Shpt$^{D61G/wt}$ and Shp2$^{D61G/D61G}$ embryos in Tg(*cd41:GFP, kdrl:mCherry-CAAX*) transgenic background at 5dpf were dissected and collected in Leibovitz-medium. After washing with PBS0 the CHTs were dissociated with TryplE (Gibco) for 45 minutes at 32°C. The resulting cell suspension was washed with PBS0, resuspended in PBS0 supplemented with 2mM EDTA, 2% FCS and 0.5µg/ml DAPI and passed through a 40µm filter. DAPI staining was used to exclude dead cells. Cells with CD41-GFP$^{low}$ positive signal were subjected to fluorescence-activated cell sorting (FACS) with an influx cytometer (BD Biosciences). Single-cell RNA sequencing was performed according to an adapted version of the SORT-seq (Muraro et al., 2016) with adapted primers described in(Van Den Brink et al., 2017). In short, single cells were FACS sorted, as described above, on 384-well plates containing 384 primers and Mineral oil (Sigma). After sorting, plates were snap-frozen on dry ice and stored at -80°C. For amplification cells were heat-lysed at 65°C followed by cDNA synthesis using the CEL-seq2 (Hashimshony et al., 2016) and robotic liquid handling platforms. After the second strand cDNA synthesis, the barcoded material was pooled into libraries of 384 cells and amplified using IVT. Following amplification, the rest of the CEL-seq2 protocol was followed for preparation of the amplified cDNA library, using TruSeq small RNA primers (Illumina). The DNA library was paired-end sequenced on an Illumina Nextseq™ 500, high output, with a 1x75 bp Illumina kit (R1:26 cycles, index read: 6 cycles, R2:60 cycles).

## Colony forming assay

Whole kidney marrows (WKMs) of the three adult Shp2$^{wt}$, Shp2$^{D61G/wt}$ and Shp2$^{D61G/D61G}$ siblings in the Tg*(mpx:GFP, mpeg:mCherry)* transgenic background were dissected and collected in PBS supplemented with 5% FBS. The tissue was mechanically dissociated and filtered through a 70 µm and 40 µm filter. Cell pellet was resuspended in PBS supplemented with 5% FBS. 1.6 ml of solution containing 20 000 cells in media, which was prepared as described in (Svoboda et al., 2016)**,** and 100 ng/ml of granulocyte colony stimulating factor a and b (Gscfa and Gcsfb, gift from the Petr Bartunek lab, Institute of Molecular Genetics, Academy of Sciences of the Czech Republic v.v.i. Prague) was plated per well of a 12 well plate in a duplicate. Cells were grown in humidified incubators at 32°C, 5% $CO_2$. After 2 days, using the EVOS microscope (Termo Fischer Scientific) colonies were imaged, examined for the presence of GFP and mCherry fluorescence and enumerated.

## Transplantation experiments

Zebrafish kidney marrow transplantation were performed as previously described (Moore et al., 2016b; Tang et al., 2014). In short, tissues were isolated from donor Shp2$^{D61G/wt}$ or wild type animals in the Tg(*mpx:GFP, mpeg:mCherry*) background following Tricaine (Western Chemical) overdose. Excised tissues from dissected fish are placed into 500 µl of 0.9x PBS + 5% FBS on a 10-cm Petri dish. Single-cell suspensions were obtained by maceration with a razor blade, followed by manual pipetting to disassociate cell clumps. Cells were filtered through a 40-µm filter (Falcon), centrifuged at 1,000 *g* for 10 min, and resuspended to the 2 x $10^7$ cells/ml. 5-µl suspension containing $10^5$ kidney marrow cells were injected into the peritoneal cavity

of each recipient fish using a 26s Hamilton 80366 syringe. Cellular engraftment was assessed at 0, 7, 14, 28 dpt by epifluorescence microscopy.

## Quantification and Statistical Analysis

### Statistical analysis

Data was plotted in GraphPad Prism 7.05, except for the violin plots of gene expression, which were plotted in R using ggplot2 (Wickham, 2009). Statistical difference analysis was performed using the one-way ANOVA supplemented by Tukey's HSD test in GraphPad Prism 7.05, except for the gene expression differences in single cell RNA sequencing data, where T-test was performed in R, and the treatment WISH experiments, where Chi-squared test was performed in GraphPad Prism 7.05. Significant difference was considered when $p<0.05$ (*$p<0.05$, **$p<0.01$, ***$p<0.001$, NS=non significant).

### Data analysis of single-cell RNA sequencing

During sequencing, Read1 was assigned 26 base pairs and was used for identification of the Ilumina library barcode, cell barcode and unique molecular identifier (UMI). Read2 was assigned 60 base pairs and used to map to the reference transcriptome of Zv9 Danio rerio. Data was demultiplexed as described in (Grün et al., 2014). Single cell transcriptomics analysis was done using the RaceID3 algorithm(Herman et al., 2018), following an adapted version of the RaceID manual (https://cran.r-project.org/web/packages/RaceID/vignettes/RaceID.html) using R-3.5.2. In total 768 cells per genotype were sequenced for the datasets. After removing cells with less than 1000 UMIs and only keeping genes that were detected with al least 3 UMIs in 1 cell,

439 wt, 384 D61G/wt and 543 D61G/D61G cells were left for further analysis. Batch effects observed for plates which were prepared on different days was removed using the scran function. 4 major clusters and 5 minor clusters were identified. The minor clusters contained 130 cells in total and were excluded from further analysis for statistical reasons.

Differential gene expression analysis was done as described in (Muraro et al., 2016) with an adapted version of the DESseq2 (Love et al., 2014). GO term enrichment analysis for differentially expressed genes of each major cluster was performed using the DAVID Bioinformatics Resources 6.8 (https://david.ncifcrf.gov/).

# References

Araki, T., Mohi, M.G., Ismat, F.A., Bronson, R.T., Williams, I.R., Kutok, J.L., Yang, W., Pao, L.I., Gilliland, D.G., Epstein, J.A., et al. (2004). Mouse model of Noonan syndrome reveals cell type- and gene dosage-dependent effects of Ptpn11 mutation. Nat. Med. *10*, 849–857.

Araki, T., Chan, G., Newbigging, S., Morikawa, L., Bronson, R., and Neel, B.G. (2009). Noonan syndrome cardiac defects are caused by PTPN11 acting in endocardium to enhance endocardial-mesenchymal transformation. Proc. Natl. Acad. Sci. U. S. A. *106*, 4736–4741.

Arranz, L., Arriero, M. del M., and Villatoro, A. (2017). Interleukin-1β as emerging therapeutic target in hematological malignancies and potentially in their complications. Blood Rev. *31*, 306–317.

Athanasiadis, E.I., Botthof, J.G., Andres, H., Ferreira, L., Lio, P., and Cvejic, A. (2017). Single-cell RNA-sequencing uncovers transcriptional states and fate decisions in haematopoiesis. Nat. Commun. *8*, 2045.

Bagby, G.C., Dinarello, C.A., Neerhout, R.C., Ridgway, D., and McCall, E. (1988). Interleukin 1-dependent paracrine granulopoiesis in chronic granulocytic leukemia of the juvenile type. J. Clin. Invest. *82*, 1430–1436.

Bonetti, M., Rodriguez-Martinez, V., Overman, J.P., Overvoorde, J., Van Eekelen, M., Jopling, C., and Den Hertog, J. (2014). Distinct and overlapping functions of ptpn11 genes in zebrafish development. PLoS One *9*, e94884.

Van Den Brink, S.C., Sage, F., Vértesy, Á., Spanjaard, B., Peterson-Maduro, J., Baron, C.S., Robin, C., and Van Oudenaarden, A. (2017). Single-cell sequencing reveals dissociation-induced gene expression in tissue subpopulations. Nat. Methods *14*, 935–936.

Chang, T.Y., Dvorak, C.C., and Loh, M.L. (2014). Bedside to bench in juvenile myelomonocytic leukemia: insights into leukemogenesis from a rare pediatric leukemia. Blood *124*, 2487–2497.

Choorapoikayil, S., Kuiper, R. V, de Bruin, A., and den Hertog, J. (2012). Haploinsufficiency of the genes encoding the tumor suppressor Pten predisposes zebrafish to hemangiosarcoma. Dis. Model. Mech. *5*, 241–247.

Choorapoikayil, S., Kers, R., Herbomel, P., Kissa, K., and den Hertog, J. (2014). Pivotal role of Pten in the balance between proliferation and differentiation of hematopoietic stem cells in zebrafish. Blood *123*, 184–190.

Craver, B.M., El Alaoui, K., Scherber, R.M., and Fleischman, A.G. (2018). The critical

role of inflammation in the pathogenesis and progression of myeloid malignancies. Cancers (Basel). *10*.

Dong, L., Yu, W.M., Zheng, H., Loh, M.L., Bunting, S.T., Pauly, M., Huang, G., Zhou, M., Broxmeyer, H.E., Scadden, D.T., et al. (2016). Leukaemogenic effects of Ptpn11 activating mutations in the stem cell microenvironment. Nature *539*, 304–308.

Ellett, F., Pase, L., Hayman, J.W., Andrianopoulos, A., and Lieschke, G.J. (2011). mpeg1 promoter transgenes direct macrophage-lineage expression in zebrafish. Blood *117*, e49.

Emanuel, P.D., Bates, L.J., Castleberry, R.P., Gualtieri, R.J., and Zuckerman, K.S. (1991). Selective hypersensitivity to granulocyte-macrophage colony-stimulating factor by juvenile chronic myeloid leukemia hematopoietic progenitors. Blood *77*, 925–929.

Freedman, M.H., Cohen, A., Grunberger, T., Bunin, N., Luddy, R.E., Saunders, E.F., Shahidi, N., Lau, A., and Estrov, Z. (1992). Central role of tumour necrosis factor, GM-CSF, and interleukin 1 in the pathogenesis of juvenile chronic myelogenous leukaemia. Br. J. Haematol. *80*, 40–48.

Gagnon, J.A., Valen, E., Thyme, S.B., Huang, P., Akhmetova, L., Ahkmetova, L., Pauli, A., Montague, T.G., Zimmerman, S., Richter, C., et al. (2014). Efficient mutagenesis by Cas9 protein-mediated oligonucleotide insertion and large-scale assessment of single-guide RNAs. PLoS One *9*, e98186.

Gelb, B.D., and Tartaglia, M. (2006). Noonan syndrome and related disorders: dysregulated RAS-mitogen activated protein kinase signal transduction. Hum. Mol. Genet. *15*, R220–R226.

Grün, D., Kester, L., and Van Oudenaarden, A. (2014). Validation of noise models for single-cell transcriptomics. Nat. Methods *11*, 637–640.

Hale, A.J., and den Hertog, J. (2017). Shp2–Mitogen-Activated Protein Kinase Signaling Drives Proliferation during Zebrafish Embryo Caudal Fin Fold Regeneration. Mol. Cell. Biol. *38*.

Hamarsheh, S., Osswald, L., Saller, B.S., Unger, S., De Feo, D., Vinnakota, J.M., Konantz, M., Uhl, F.M., Becker, H., Lübbert, M., et al. (2020). Oncogenic KrasG12D causes myeloproliferation via NLRP3 inflammasome activation. Nat. Commun. *11*, 12.

Hashimshony, T., Senderovich, N., Avital, G., Klochendler, A., de Leeuw, Y., Anavy, L., Gennert, D., Li, S., Livak, K.J., Rozenblatt-Rosen, O., et al. (2016). CEL-Seq2: Sensitive highly-multiplexed single-cell RNA-Seq. Genome Biol. *17*, 77.

Herman, J.S., Sagar, and Grün, D. (2018). FateID infers cell fate bias in multipotent progenitors from single-cell RNA-seq data. Nat. Methods *15*, 379–386.

Hernández-Porras, I., Jiménez-Catalán, B., Schuhmacher, A.J., and Guerra, C. (2015).

The impact of the genetic background in the Noonan syndrome phenotype induced by K-Ras(V14I). Rare Dis. (Austin, Tex.) *3*, e1045169.

Hogan, B.M., Bos, F.L., Bussmann, J., Witte, M., Chi, N.C., Duckers, H.J., and Schulte-Merker, S. (2009). Ccbe1 is required for embryonic lymphangiogenesis and venous sprouting. Nat. Genet. *41*, 396–398.

Hu, B., Zhang, W., Feng, X., Ji, W., Xie, X., and Xiao, W. (2014). Zebrafish eaf1 suppresses foxo3b expression to modulate transcriptional activity of gata1 and spi1 in primitive hematopoiesis. Dev. Biol. *388*, 81–93.

Jindal, G.A., Goyal, Y., Burdine, R.D., Rauen, K.A., and Shvartsman, S.Y. (2015). RASopathies: Unraveling mechanisms with animal models. DMM Dis. Model. Mech. *8*, 769–782.

Jopling, C., Van Geemen, D., and Den Hertog, J. (2007). Shp2 knockdown and noonan/LEOPARD mutant Shp2-induced gastrulation defects. PLoS Genet. *3*, e225.

Karnik, R., and Geiger, M. (2019). Cardiac Manifestations of Noonan Syndrome. Pediatr. Endocrinol. Rev. *16*, 471–476.

Kratz, C.P., Niemeyer, C.M., Castleberry, R.P., Cetin, M., Bergsträsser, E., Emanuel, P.D., Hasle, H., Kardos, G., Klein, C., Kojima, S., et al. (2005). The mutational spectrum of PTPN11 in juvenile myelomonocytic leukemia and Noonan syndrome/myeloproliferative disease. Blood *106*, 2183–2185.

Lin, H.F., Traver, D., Zhu, H., Dooley, K., Paw, B.H., Zon, L.I., and Handin, R.I. (2005). Analysis of thrombocyte development in CD41-GFP transgenic zebrafish. Blood *106*, 3803–3810.

Liu, K., Petree, C., Requena, T., Varshney, P., and Varshney, G.K. (2019). Expanding the CRISPR toolbox in zebrafish for studying development and disease. Front. Cell Dev. Biol. *7*.

Locatelli, F., and Niemeyer, C.M. (2015). How I treat juvenile myelomonocytic leukemia. Blood *125*, 1083–1090.

Love, M.I., Huber, W., and Anders, S. (2014). Moderated estimation of fold change and dispersion for RNA-seq data with DESeq2. Genome Biol. *15*, 550.

Matozaki, T., Murata, Y., Saito, Y., Okazawa, H., and Ohnishi, H. (2009). Protein tyrosine phosphatase SHP-2: A proto-oncogene product that promotes Ras activation. Cancer Sci. *100*, 1786–1793.

Monte Westerfield (2000). The Zebrafish Book: A Guide for the Laboratory Use of Zebrafish (Danio Rerio)  (University of Oregon Press).

Moore, J.C., Tang, Q., Yordán, N.T., Moore, F.E., Garcia, E.G., Lobbardi, R.,

Ramakrishnan, A., Marvin, D.L., Anselmo, A., Sadreyev, R.I., et al. (2016a). Single-cell imaging of normal and malignant cell engraftment into optically clear prkdc-null scid zebrafish. J. Exp. Med. *213*, 2575–2589.

Moore, J.C., Tang, Q., Yordán, N.T., Moore, F.E., Garcia, E.G., Lobbardi, R., Ramakrishnan, A., Marvin, D.L., Anselmo, A., Sadreyev, R.I., et al. (2016b). Single-cell imaging of normal and malignant cell engraftment into optically clear prkdc-null scid zebrafish. J. Exp. Med. *213*, 2575–2589.

Muraro, M.J., Dharmadhikari, G., Grün, D., Groen, N., Dielen, T., Jansen, E., van Gurp, L., Engelse, M.A., Carlotti, F., de Koning, E.J.P., et al. (2016). A Single-Cell Transcriptome Atlas of the Human Pancreas. Cell Syst. *3*, 385-394.e3.

Niemeyer, C.M., and Flotho, C. (2019). Juvenile myelomonocytic leukemia: Who's the driver at the wheel? Blood *133*, 1060–1070.

Niihori, T., Nagai, K., Fujita, A., Ohashi, H., Okamoto, N., Okada, S., Harada, A., Kihara, H., Arbogast, T., Funayama, R., et al. (2019). Germline-Activating RRAS2 Mutations Cause Noonan Syndrome. Am. J. Hum. Genet. *104*, 1233–1240.

Ogryzko, N. V., Lewis, A., Wilson, H.L., Meijer, A.H., Renshaw, S.A., and Elks, P.M. (2018). Hif-1α–Induced Expression of Il-1β Protects against Mycobacterial Infection in Zebrafish. J. Immunol.

Paardekooper Overman, J., Yi, J.-S., Bonetti, M., Soulsby, M., Preisinger, C., Stokes, M.P., Hui, L., Silva, J.C., Overvoorde, J., Giansanti, P., et al. (2014). PZR Coordinates Shp2 Noonan and LEOPARD Syndrome Signaling in Zebrafish and Mice. Mol. Cell. Biol. *34*, 2874–2889.

Pandey, R., Saxena, M., and Kapur, R. (2017). Role of SHP2 in hematopoiesis and leukemogenesis. Curr. Opin. Hematol. *24*, 307–313.

Patterson, V.L., and Burdine, R.D. (2020). Swimming toward solutions: Using fish and frogs as models for understanding RASopathies. Birth Defects Res. *112*, 749–765.

Pietras, E.M., Mirantes-Barbeito, C., Fong, S., Loeffler, D., Kovtonyuk, L. V., Zhang, S., Lakshminarasimhan, R., Chin, C.P., Techner, J.M., Will, B., et al. (2016). Chronic interleukin-1 exposure drives haematopoietic stem cells towards precocious myeloid differentiation at the expense of self-renewal. Nat. Cell Biol. *18*, 607–618.

Rauen, K.A. (2013). The RASopathies. Annu. Rev. Genomics Hum. Genet *14*, 355–369.

Renshaw, S.A., Loynes, C.A., Trushell, D.M.I., Elworthy, S., Ingham, P.W., and Whyte, M.K.B. (2006). A transgenic zebrafish model of neutrophilic inflammation. Blood *108*, 3976–3978.

Riordan, J.D., and Nadeau, J.H. (2017). From Peas to Disease: Modifier Genes,

Network Resilience, and the Genetics of Health. Am. J. Hum. Genet. *101*, 177–191.

Roberts, A.E., Allanson, J.E., Tartaglia, M., and Gelb, B.D. (2013). Noonan syndrome. Lancet (London, England) *381*, 333–342.

Runtuwene, V., van Eekelen, M., Overvoorde, J., Rehmann, H., Yntema, H.G., Nillesen, W.M., van Haeringen, A., van der Burgt, I., Burgering, B., and den Hertog, J. (2011). Noonan syndrome gain-of-function mutations in NRAS cause zebrafish gastrulation defects. Dis. Model. Mech. *4*, 393–399.

Sanchez-Vega, F., Mina, M., Armenia, J., Chatila, W.K., Luna, A., La, K.C., Dimitriadoy, S., Liu, D.L., Kantheti, H.S., Saghafinia, S., et al. (2018). Oncogenic Signaling Pathways in The Cancer Genome Atlas. Cell *173*, 321-337.e10.

Strullu, M., Caye, A., Lachenaud, J., Cassinat, B., Gazal, S., Fenneteau, O., Pouvreau, N., Pereira, S., Baumann, C., Contet, A., et al. (2014). Juvenile myelomonocytic leukaemia and Noonan syndrome. J. Med. Genet. *51*, 689–697.

Svoboda, O., Stachura, D.L., MacHonova, O., Zon, L.I., Traver, D., and Bartunek, P. (2016). Ex vivo tools for the clonal analysis of zebrafish hematopoiesis. Nat. Protoc. *11*, 1007–1020.

Tajan, M., de Rocca Serra, A., Valet, P., Edouard, T., and Yart, A. (2015). SHP2 sails from physiology to pathology. Eur. J. Med. Genet. *58*, 509–525.

Tajan, M., Paccoud, R., Branka, S., Edouard, T., and Yart, A. (2018). The RASopathy Family: Consequences of Germline Activation of the RAS/MAPK Pathway. Endocr. Rev. *39*, 676–700.

Tang, Q., Abdelfattah, N.S., Blackburn, J.S., Moore, J.C., Martinez, S.A., Moore, F.E., Lobbardi, R., Tenente, I.M., Ignatius, M.S., Berman, J.N., et al. (2014). Optimized cell transplantation using adult rag2 mutant zebrafsh. Nat. Methods *11*, 821–824.

Tartaglia, M., Mehler, E.L., Goldberg, R., Zampino, G., Brunner, H.G., Kremer, H., Van der Burgt, I., Crosby, A.H., Ion, A., Jeffery, S., et al. (2001). Mutations in PTPN11, encoding the protein tyrosine phosphatase SHP-2, cause Noonan syndrome. Nat. Genet. *29*, 465–468.

Tartaglia, M., Kalidas, K., Shaw, A., Song, X., Musat, D.L., Van der Burgt, I., Brunner, H.G., Bertola, D.R., Crosby, A., Ion, A., et al. (2002). PTPN11 mutations in noonan syndrome: Molecular spectrum, genotype-phenotype correlation, and phenotypic heterogeneity. Am. J. Hum. Genet. *70*, 1555–1563.

Tessadori, F., van Weerd, J.H., Burkhard, S.B., Verkerk, A.O., de Pater, E., Boukens, B.J., Vink, A., Christoffels, V.M., and Bakkers, J. (2012). Identification and Functional Characterization of Cardiac Pacemaker Cells in Zebrafish. PLoS One *7*, e47644.

Tessadori, F., Roessler, H.I., Savelberg, S.M.C., Chocron, S., Kamel, S.M., Duran, K.J.,

van Haelst, M.M., van Haaften, G., and Bakkers, J. (2018). Effective CRISPR/Cas9-based nucleotide editing in zebrafish to model human genetic cardiovascular disorders. Dis. Model. Mech. *11*.

Thisse, C., Thisse, B., Schilling, T.F., and Postlethwait, J.H. (1993). Structure of the zebrafish snail1 gene and its expression in wild-type, spadetail and no tail mutant embryos. Development *119*.

Wickham, H. (2009). ggplot2: Elegant Graphics for Data Analysis (Springer International Publishing).

Xu, D., Wang, S., Yu, W.-M., Chan, G., Araki, T., Bunting, K.D., Neel, B.G., and Qu, C.-K. A germline gain-of-function mutation in Ptpn11 (Shp-2) phosphatase induces myeloproliferative disease by aberrant activation of hematopoietic stem cells.

Xu, D., Wang, S., Yu, W.-M., Chan, G., Araki, T., Bunting, K.D., Neel, B.G., and Qu, C.-K. (2010a). A germline gain-of-function mutation in Ptpn11 (Shp-2) phosphatase induces myeloproliferative disease by aberrant activation of hematopoietic stem cells. Blood *116*, 3611–3621.

Xu, D., Wang, S., Yu, W.-M., Chan, G., Araki, T., Bunting, K.D., Neel, B.G., and Qu, C.-K. (2010b). A germline gain-of-function mutation in Ptpn11 (Shp-2) phosphatase induces myeloproliferative disease by aberrant activation of hematopoietic stem cells. Blood *116*, 3611–3621.

Zhao, W., Wang, L., and Yu, Y. (2018). Gene module analysis of juvenile myelomonocytic leukemia and screening of anticancer drugs. Oncol. Rep. *40*, 3155–3170.

# Figure 1:

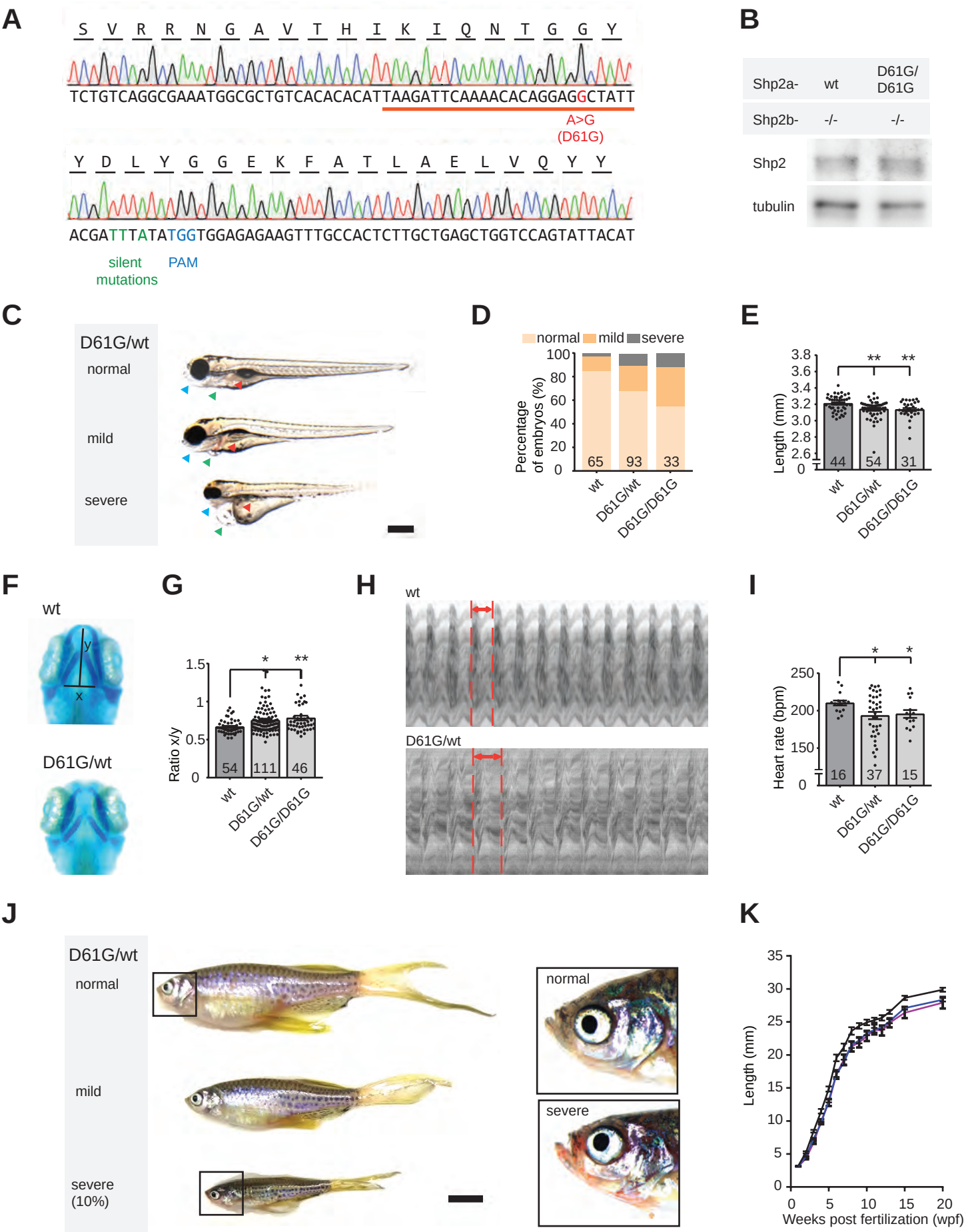
A
S V R R N G A V T H I K I Q N T G G Y
TCTGTCAGGCGAAATGGCGCTGTCACACACATTAAGATTCAAAACACAGGAGGCTATT
A>G
(D61G)
Y D L Y G G E K F A T L A E L V Q Y Y
ACGATTTATATGGTGGAGAGAAGTTTGCCACTCTTGCTGAGCTGGTCCAGTATTACAT
silent mutations
PAM
B
Shp2a- wt D61G/D61G
Shp2b- -/- -/-
Shp2
tubulin
C
D61G/wt
normal
mild
severe
D
normal mild severe
Percentage of embryos (%)
65 93 33
wt D61G/wt D61G/D61G
E
Length (mm)
44 54 31
wt D61G/wt D61G/D61G
F
wt
D61G/wt
G
Ratio x/y
54 111 46
wt D61G/wt D61G/D61G
H
wt
D61G/wt
I
Heart rate (bpm)
16 37 15
wt D61G/wt D61G/D61G
J
D61G/wt
normal
mild
severe (10%)
normal
severe
K
Length (mm)
Weeks post fertilization (wpf)

# Figure 2:

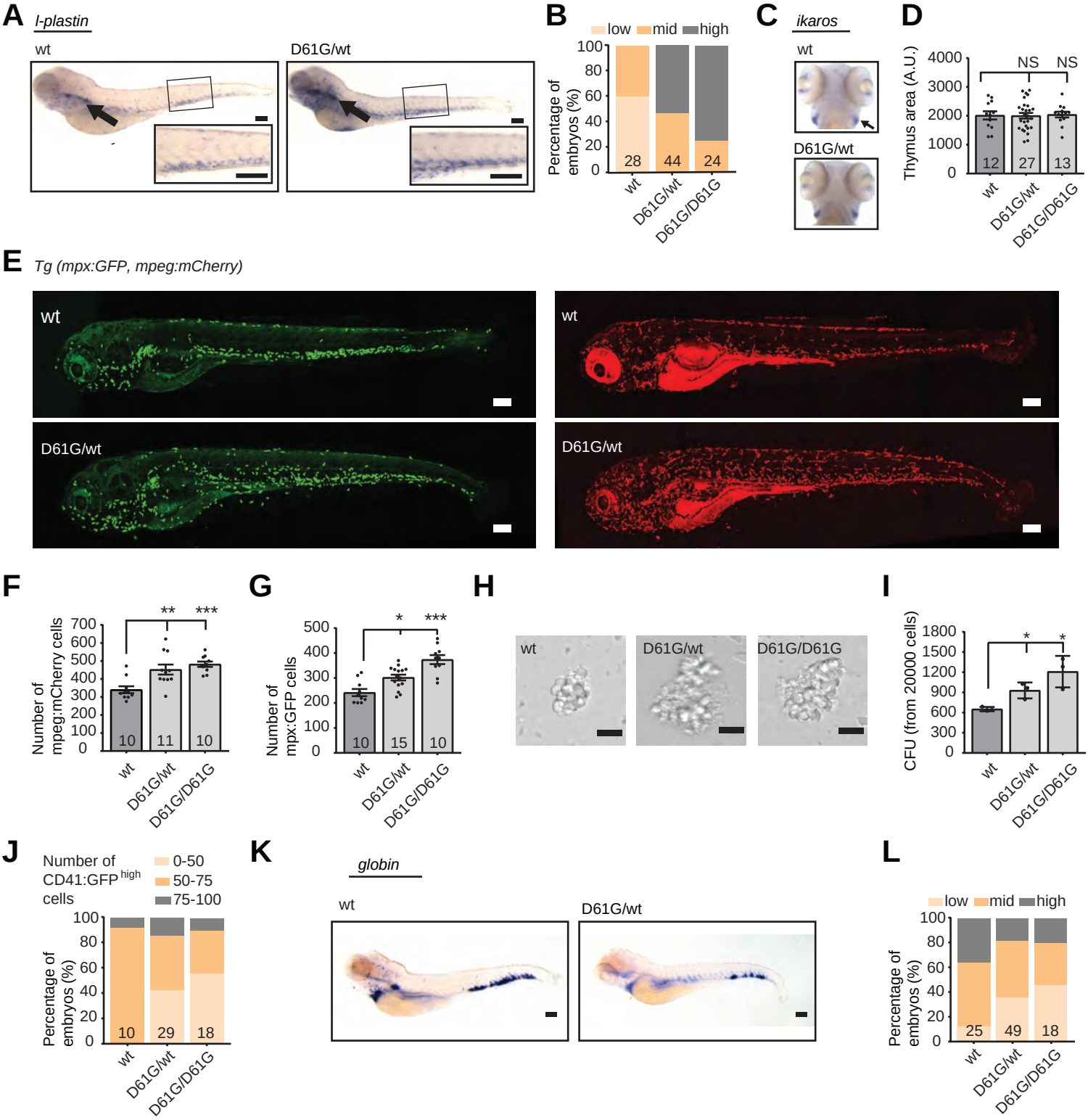
A
l-plastin
wt
D61G/wt
B
low
mid
high
Percentage of embryos (%)
100
80
60
40
20
0
28
44
24
wt
D61G/wt
D61G/D61G
C
ikaros
wt
D61G/wt
D
Thymus area (A.U.)
4000
3000
2000
1000
0
NS
NS
12
27
13
wt
D61G/wt
D61G/D61G
E
Tg (mpx:GFP, mpeg:mCherry)
wt
wt
D61G/wt
D61G/wt
F
Number of mpeg:mCherry cells
700
600
500
400
300
200
100
0
**
***
10
11
10
wt
D61G/wt
D61G/D61G
G
Number of mpx:GFP cells
500
400
300
200
100
0
*
***
10
15
10
wt
D61G/wt
D61G/D61G
H
wt
D61G/wt
D61G/D61G
I
CFU (from 20000 cells)
1800
1500
1200
900
600
300
0
*
*
wt
D61G/wt
D61G/D61G
J
Number of CD41:GFP high cells
0-50
50-75
75-100
Percentage of embryos (%)
100
80
60
40
20
0
10
29
18
wt
D61G/wt
D61G/D61G
K
globin
wt
D61G/wt
L
low
mid
high
Percentage of embryos (%)
100
80
60
40
20
0
25
49
18
wt
D61G/wt
D61G/D61G

# Figure 3:

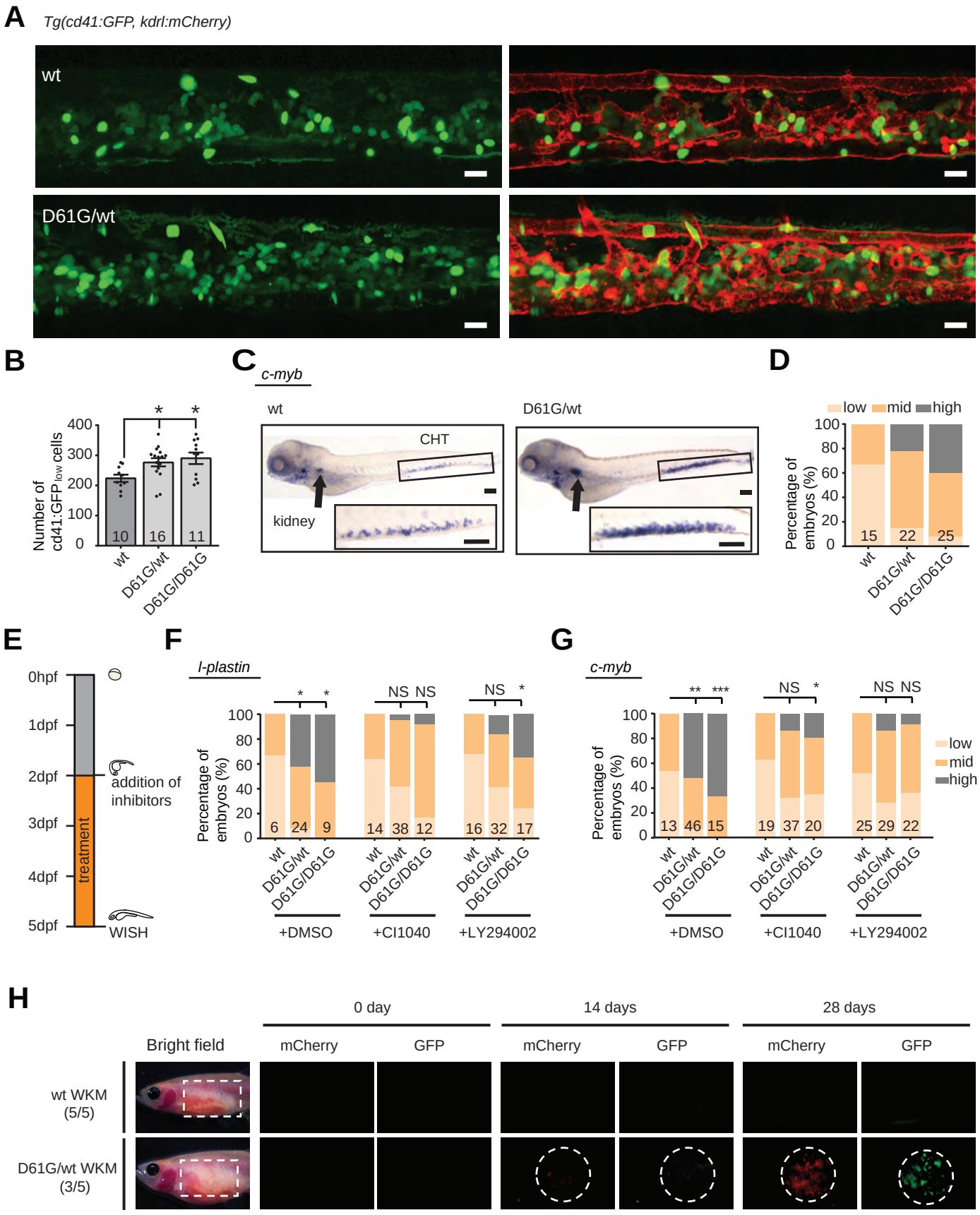
A
Tg(cd41:GFP, kdrl:mCherry)
wt
D61G/wt
B
Number of cd41:GFP low cells
400
300
200
100
0
10
16
11
wt
D61G/wt
D61G/D61G
C
c-myb
wt
D61G/wt
CHT
kidney
D
low
mid
high
Percentage of embryos (%)
100
80
60
40
20
0
15
22
25
wt
D61G/wt
D61G/D61G
E
0hpf
1dpf
2dpf
3dpf
4dpf
5dpf
treatment
addition of inhibitors
WISH
F
l-plastin
Percentage of embryos (%)
* *
NS NS
NS *
6 24 9
14 38 12
16 32 17
wt
D61G/wt
D61G/D61G
+DMSO
+CI1040
+LY294002
G
c-myb
** ***
NS *
NS NS
13 46 15
19 37 20
25 29 22
low
mid
high
H
0 day
14 days
28 days
Bright field
mCherry
GFP
wt WKM (5/5)
D61G/wt WKM (3/5)

# Figure 4:

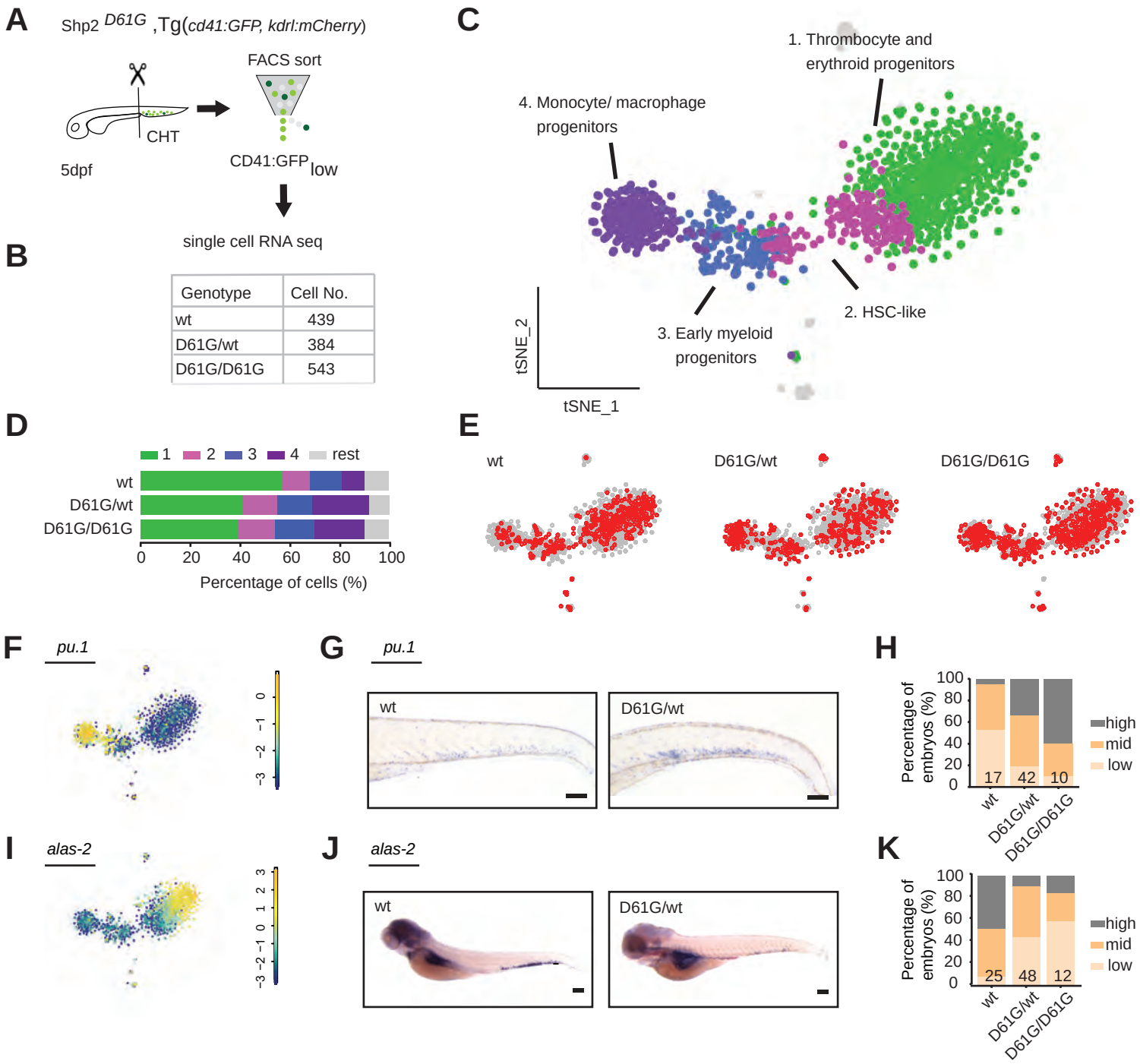


| Genotype | Cell No. |
|---|---|
| wt | 439 |
| D61G/wt | 384 |
| D61G/D61G | 543 |

# Figure 5:

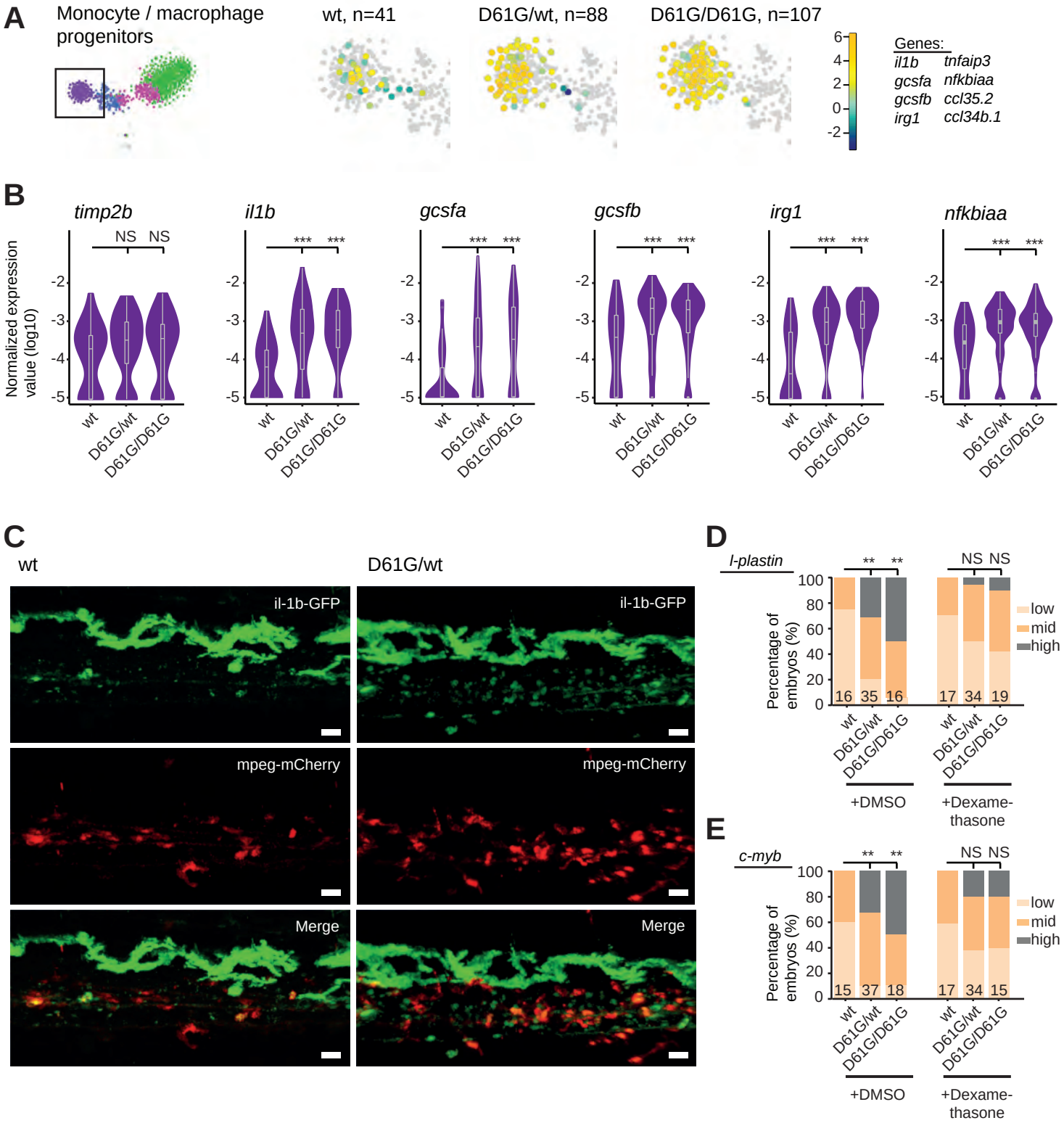
A
Monocyte / macrophage progenitors
wt, n=41
D61G/wt, n=88
D61G/D61G, n=107
6
4
2
0
-2
Genes:
il1b
gcsfa
gcsfb
irg1
tnfaip3
nfkbiaa
ccl35.2
ccl34b.1
B
timp2b
il1b
gcsfa
gcsfb
irg1
nfkbiaa
Normalized expression value (log10)
NS NS
*** ***
wt
D61G/wt
D61G/D61G
C
wt
D61G/wt
il-1b-GFP
mpeg-mCherry
Merge
D
l-plastin
** **
NS NS
Percentage of embryos (%)
low
mid
high
16 35 16
17 34 19
+DMSO
+Dexame-thasone
E
c-myb
15 37 18
17 34 15